JOURNAL OF THERMOPHYSICS AND HEAT TRANSFER
Vol. 16, No. 1, January–March 2002

Experimental Investigation of Air Radiation from Behind a Strong Shock Wave

Kazuhisa Fujita,* Sunichi Sato,† and Takashi Abe‡
Institute of Space and Astronautical Science, Kanagawa 229-8510, Japan
and
Yuta Ebinuma§
Aoyama Gakuin University, Tokyo 157-8572, Japan

Radiation phenomena behind a strong shock wave have been experimentally investigated using a free-piston double-diaphragm shock tube. The shock front is detected by pressure sensors, whose rise time is calibrated by a laser schlieren technique. Using the simulated air as the test gas, spatial distribution of the emission spectra behind the shock front is obtained for the 270–520-nm wavelength range by means of the one-dimensional spatially resolved imaging spectroscopy, in which a wavelength vs position image is taken by an image-intensified charge-coupled device camera with an exposure time of 100 ns. Molecular spectra of the N_2 (2+) and the N_2^+ (1−) system are seen shortly after the shock front, whereas mainly the atomic line spectra from N are seen afterwards. Using pure nitrogen as the test gas, the rotational and vibrational temperatures of the molecules and the electronic excitation temperature of the atoms are determined, and their spatial distribution is obtained for a shock velocity of 11.9 km/s at an ambient pressure of 0.3 torr. The measured temperatures are in significant nonequilibrium with the translational temperature. Also, the temperatures of N_2^+ are much higher than those of N_2.

Nomenclature

A_{ij} = Einstein A coefficient of $i - j$ transition, s^{-1}
g_i = statistical weight of i state
I_{ij} = relative radiation intensity of $i - j$ transition, photon · nm^{-1}
L = distance from shock front, mm
P_0 = ambient pressure ahead of shock wave, torr
T_e = electronic excitation temperature, K
T_r = rotational temperature, K
T_v = vibrational temperature, K
V = incident shock velocity, km/s

Introduction

NONEQUILIBRIUM aerothermodynamic phenomena behind a strong shock wave encountered by the vehicles reentering the planetary atmospheres have been vigorously investigated to date both experimentally and theoretically. As a consequence of these studies, thermochemical models for reentry calculation have been developed, which are recently summarized in Refs. 1–4, for example.

Computational-fluid-dynamic results obtained by the latest thermochemical models show fairly good agreement among each other and also with the experiment at moderate reentry speeds below 8 km/s. Accuracy of these models has been demonstrated by comparing the computed heat fluxes, electron number densities, and emission spectra with the experimental values. From a vehicle design standpoint prediction of the aerodynamic forces and the heat fluxes is of primary importance to protect successfully the vehicles from the severe reentry environment. Recent flight experiments agree well with the latest model predictions for this reentry speed range.[5]

However, if we apply these aerothermodynamic models to higher reentry velocities the results show significant differences. In the case of MUSES-C reentry capsule,[6,7] which is currently designed to reenter the Earth's atmosphere directly from the interplanetary orbit at a velocity over 12 km/s, the stagnation-point heating rate is found to depend strongly on the models used in the analysis. Especially the radiative heat flux, whose contribution to total heating of the capsule is high in this speed range, varies by an order of magnitude according to the thermochemical models used in the analysis.[8,9] It seems that the nonequilibrium aerothermochemistry behind a strong shock wave is not understood well in the velocity range over 10 km/s. The present study is directed toward an assessment of the latest thermochemical models, for the purpose of extending their applicability to a very high-speed flight regime to be encountered by the MUSES-C reentry capsule.

There are several possible experimental approaches for the investigation of the nonequilibrium thermochemistry behind a strong shock wave. Among them, the shock-tube experiment has an advantage that it can produce a known flow environment behind the shock wave, although the time allowed for a measurement is limited. In obtaining the thermochemical information from behind the shock wave in a short experimental time available, spectroscopic measurement is effective. Because the thermochemical properties vary with the distance from the shock front, it is necessary first to determine the shock front precisely, and then to obtain spectroscopic data as a function of the distance from the shock front.

Experimental Method

Experimental investigations are conducted using a free-piston double-diaphragm shock tube at the Institute of Space and Astronautical Science.[10] The last stage of the shock tube downstream of the second diaphragm, in which the test section is located, is made of aluminum alloy so that impurity in the test gas, consisting of iron, can be reduced.[4] The shock tube can generate a strong shock wave with a maximum velocity of 14 km/s in the ambient air at 0.3 torr, which covers all possible MUSES-C entry conditions. The cross section of the test section is a 35.4 × 35.4 mm square, and quartz

Presented as Paper 98-2467 at the AIAA/ASME 7th Joint Thermophysics and Heat Transfer Conference, Albuquerque, NM, 15–18 June 1998; received 29 June 2001; revision received 11 October 2001; accepted for publication 12 October 2001.

*Research Associate, 3-1-1 Yoshinodai, Sagamihara. Member AIAA.
†Technical Official, 3-1-1 Yoshinodai, Sagamihara. Member AIAA.
‡Professor, 3-1-1 Yoshinodai, Sagamihara. Senior Member AIAA.
§Graduate Student, Department of Mechanical Engineering, Chitosedai 6-16-1, Setagaya.

windows are mounted on the side walls to enable observation of radiation from the test gas. The preliminary study of the shock-tube flow has shown that the image of the radiating gas obtained in this facility can be regarded one dimensional in the streamwise direction with sufficient accuracy.[10]

Laser Schlieren Diagnostics

The shock arrival is detected by means of the laser schlieren technique. The experimental setup of the laser schlieren system is shown in Fig. 1. A pin photodiode with a 400–1080-nm spectral sensitivity and a 50-ns rise time is located sufficiently far from the mirror so that the system can be sensitive to a deflection of the laser beam caused by the density gradient at the shock front. To exclude the gas radiation reaching the photodiode, the quartz window is covered with a shield disk with holes. The holes are located along a line perpendicular to the shock-tube axis. The plane perpendicular to the shock-tube axis intersecting the holes will be denoted hereafter the test plane. A He-Ne laser beam is aligned to pass in the test plane, one of the holes on the shield disk, a hole on a guard plate, and a bandpass filter placed between the mirror and the pin photodiode.

The gas radiation from behind the shock wave is measured by another pin photodiode through a different hole. A ray from the test plane passes this hole and the holes on two additional guard plates. In addition, a quick-response pressure sensor (PCB piezotronics Inc. model 113A21), which is denoted as PS1 in Fig. 1, is installed in the test plane. Output signals from the pin photodiodes and the pressure sensor are recorded on a digital oscilloscope with the temporal resolution of 1 ns.

Spatially Resolved Imaging Spectroscopy

To obtain a spatial profile of gas radiation in the streamwise direction, a spatially resolved imaging spectroscopy is performed, as illustrated schematically in Fig. 2. The field of the radiating gas is focused by a quartz lens on the entrance slit of the spectrometer so that the slit is aligned with the axis of the shock-tube flow. The linear image formed at the entrance slit is then separated into its spectral components by an ORIEL MS127i imaging spectrometer, which generates a two-dimensional image (distance along the slit in one dimension and wavelength in the other dimension) on the photosensitive surface of an ANDOR InstaSpecV IS510 image-intensified CCD (ICCD) camera attached to the spectrometer. The spatial resolution of this system is less than 1.1 mm in the present measurement.

The ICCD camera is gated by a Stanford Research Systems DG-535 pulse generator with an exposure time of 100 ns. Trigger timing is controlled by an output signal of another pressure sensor (PS2 in Fig. 1) positioned at the 68.5 mm upstream point of the PS1 sensor.

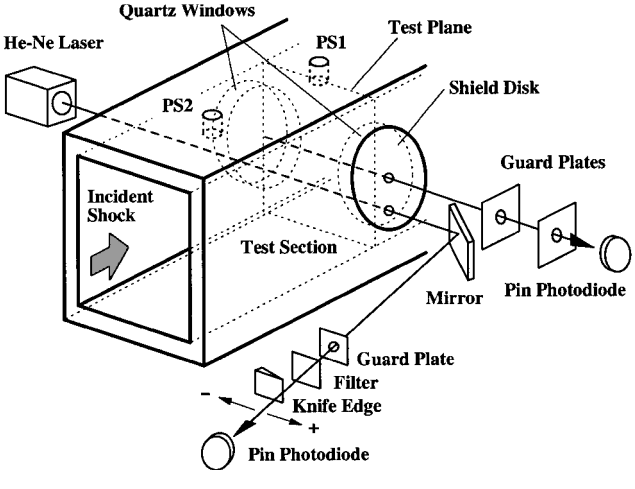

Fig. 1 Experimental setup of laser schlieren system.

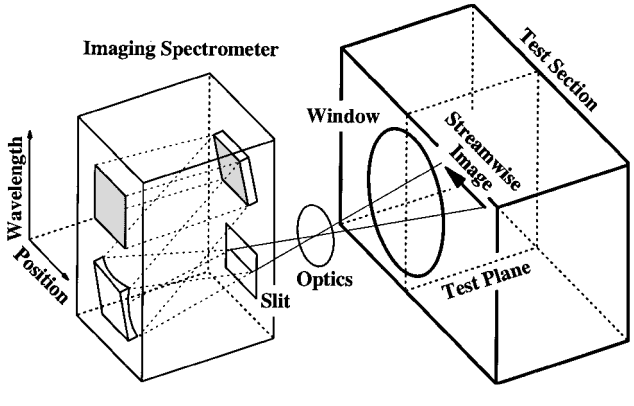

Fig. 2 Schematic view of spatially resolved imaging spectroscopy.

Experimental Results

Shock Front Detection

The shock tube is driven using the simulated air composed of 78.7% nitrogen and 21.3% oxygen in mole fraction in the test section to exclude the emission from impurities such as the water vapor, carbon dioxide, and other chemical species. Relative values of the peak radiation intensity from behind the shock wave measured by the pin photodiode are plotted against the incident shock velocity V for each ambient pressure P_0 in Fig. 3. The peak radiation intensity is strongly dependent on V because V strongly influences the vibrational and electronic excitation of the gas particles. An increase in the ambient pressure also raises the peak radiation intensity because of the increase in the number densities of the radiating particles.

Output signals from the pressure sensor and the pin photodiodes are presented in Fig. 4 for several operation cases. The vertical axis shows relative values of each sensor output with an offset, and the horizontal axis is the relative time, each division representing 1 μs. The density gradient at the shock front is expected to deflect the laser beam toward the negative direction denoted by the negative sign in Fig. 1. This is the case when P_0 is relatively high and V is low. However, with decreasing P_0 and increasing V the laser beam deflects less toward the negative side but begins to deflect to the positive side, and finally, the laser beam is deflected only to the positive side. Such an opposite deflection is brought about by an increase in the charged particles produced behind the shock wave. Because the shock front is represented by an increase in gas density, the experimental results suggest that the shock front becomes undetectable by the laser schlieren measurement as V increases and P_0 decreases. In the present measurement the threshold shock velocity for shock detection is found to be 12.0 km at $P_0 = 0.3$ torr.

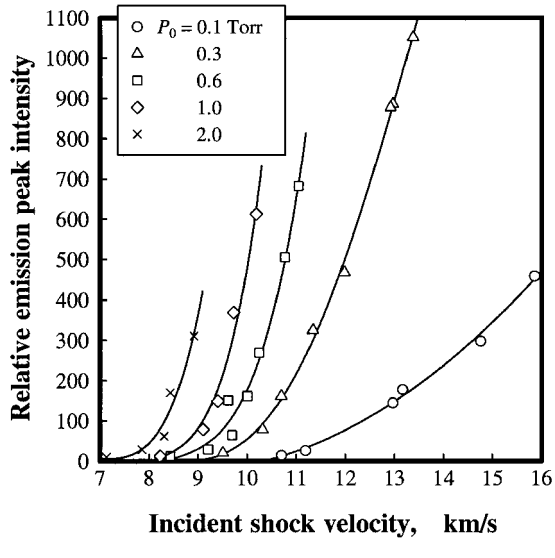

Fig. 3 Peak radiation intensity from behind the shock wave.

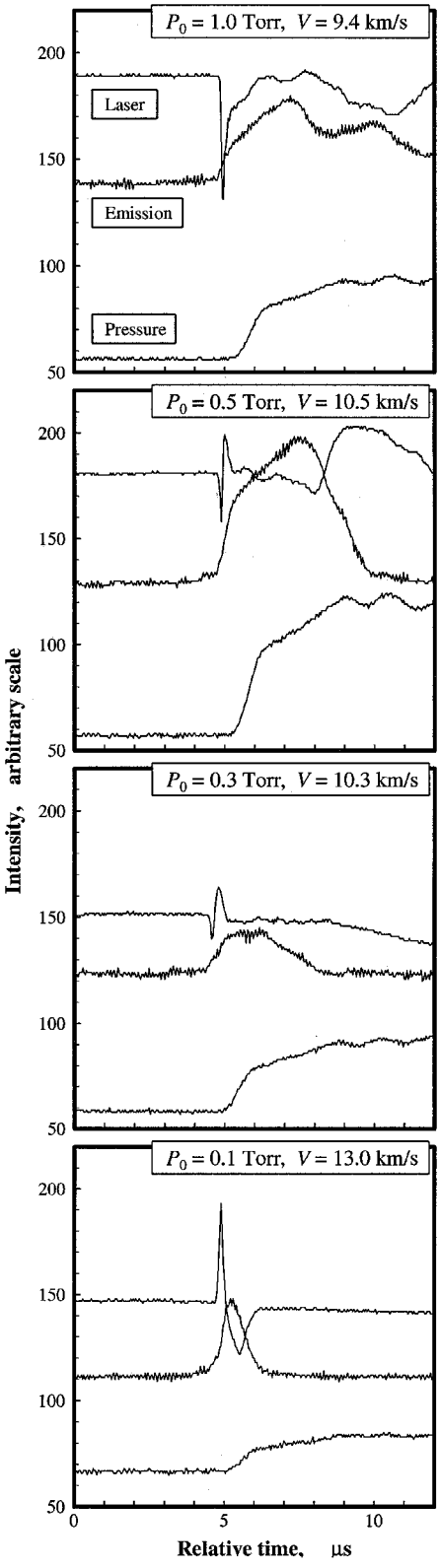

Fig. 4 Output signals from pin photodiodes and pressure sensor.

Thus, although the laser schlieren technique is generally highly sensitive, it is not suitable for the present purpose. Therefore, we use the pressure sensors to detect the shock front. The rise time of the pressure sensor, which is found to be independent of V and P_0 and reproducible over a wide range of V, is calibrated by the laser schlieren measurement. Errors in rise time of the pressure sensors are estimated to be ± 60 ns at $V = 10$–12 km/s and $P_0 = 0.3$ torr, which corresponds to spatial errors of ± 0.60–0.72 mm in detecting the shock front.

Spatial Distribution of Spectra

Figure 5 shows a variation of the emission spectrum in the streamwise direction obtained by the spatially resolved imaging spectroscopy. The simulated air is used in the test section. The incident shock velocity and the ambient pressure ahead of the shock wave are 11.9 km/s and 0.3 torr, respectively. The emission spectra are given at every 1.14 mm position in the streamwise direction. The molecular spectra of N_2 $(2+)$ and N_2^+ $(1-)$ system are seen immediately behind the shock front, while the atomic line spectra of N become noticeably prominent after 3.43 ± 0.7 mm behind the shock front. The molecular spectra are still distinguishable even at a 11.4-mm distance from the shock front. An atomic spectral line of O, which is actually composed of unresolved three lines, is also observable at around 395 nm. Intense spectral lines of the H Balmer series originating from the water vapor are also found.

In a preliminary experiment we have found that the measured spectra are substantially influenced by the impurities contained in the ambient gas of the test section, even when their mole fractions are very small. Among such impurities the water vapor and carbonic compounds have significant influences on the resultant spectra. With respect to the carbonic compounds, even $3.2 \times 10^{-2}\%$ of carbon dioxide contained in the atmospheric air can result in the CN violet band spectrum with considerable intensity. We successfully reduced this impurity contribution by using the simulated air or pure nitrogen (contained C being less than 10 ppm) instead of the atmospheric air. In addition, the existence of the carbonic compounds is monitored in the experiment by measuring the emission intensity at 247.9 nm where a strong singlet line of carbon exists.

On the other hand, the atomic lines of H cannot be completely eliminated because the water vapor inevitably adheres to the channel surface of the test section when the shock tube is exposed to the atmosphere. The contribution of the Balmer series lines and H continuum is estimated roughly by the spectral intensity of the $H(\beta)$ and the $H(\gamma)$ lines. In general, their contribution is negligibly small in the wavelength range below 430 nm.

Evaluation of Temperatures in Nitrogen Gas

Experimental Procedure

To obtain quantitative information about physical properties behind the shock wave free of the complexity in radiative phenomena caused by oxygen, pure nitrogen is used as the test gas at $P_0 = 0.3 \pm 0.001$ torr. Although the imaging spectroscopy yields qualitative information on the spatial distribution of the emission spectra at a time, it is found to be inadequate for quantitative determination of physical properties because the signal-to-noise ratio is not sufficiently high because of the low reading on each pixel of the CCD camera. This experimental difficulty is solved only by a series of pointwise spectroscopy in the following way.

To eliminate the chromatic aberration, a pair of an ellipsoidal and a flat mirror is used to get an image onto the objective slit of the imaging spectrometer. Rotation of the imaging spectrometer by 90 deg around the line of site yields a one-dimensional spectroscopic image in the direction parallel to the shock wave. By accumulating spatial components for each wavelength, a mean spectrum correlated with the distance from the shock front is obtained. Repetition of this procedure with changing the trigger timing for the ICCD camera finally yields a series of pointwise spectra correlated with the distance from the shock front.

Each spectrum obtained in this approach is subject to the spatial uniformity of radiation processes in the test plane, both in the direction parallel to the objective slit and in the direction of the line of sight. In a preliminary experiment the spatial uniformity in both directions was examined by using a quartz test plate to simulate the quartz windows of the test section: the test plate was temporarily attached to the bottom wall of the test section, and the variation of the spectrum intensity in the direction normal to the test plate was observed. At the shock velocity of $V = 11.90$ km/s, the spectra observed immediately behind the shock front were found to be uniform in the direction parallel to the shock wave to within 5% in total intensity over a 400–1080 nm range, except for the region within

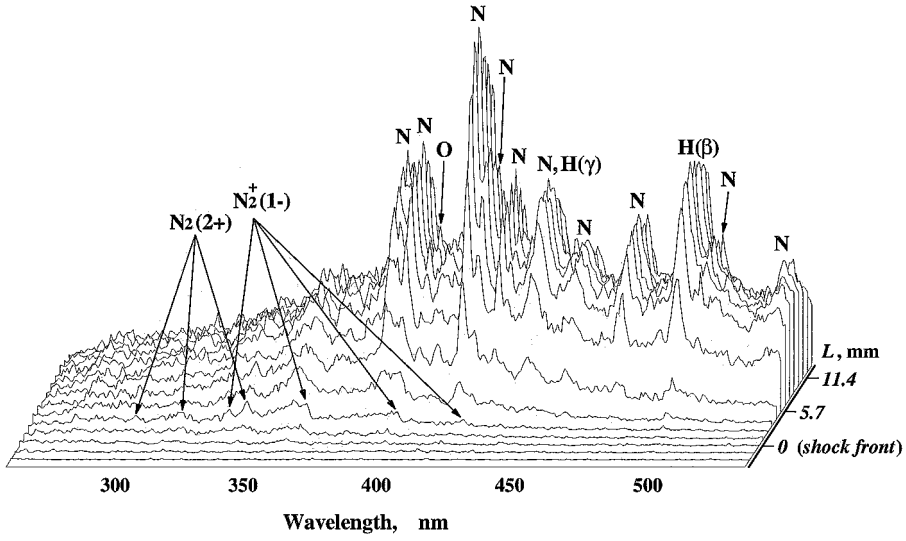

Fig. 5 Spatial variation of spectra correlated with the shock front (simulated air, $P_0 = 0.3$ torr, $V = 11.9$ km/s, and spectral resolution = 0.69 nm/pixel; spectra are given at every 1.14 mm).

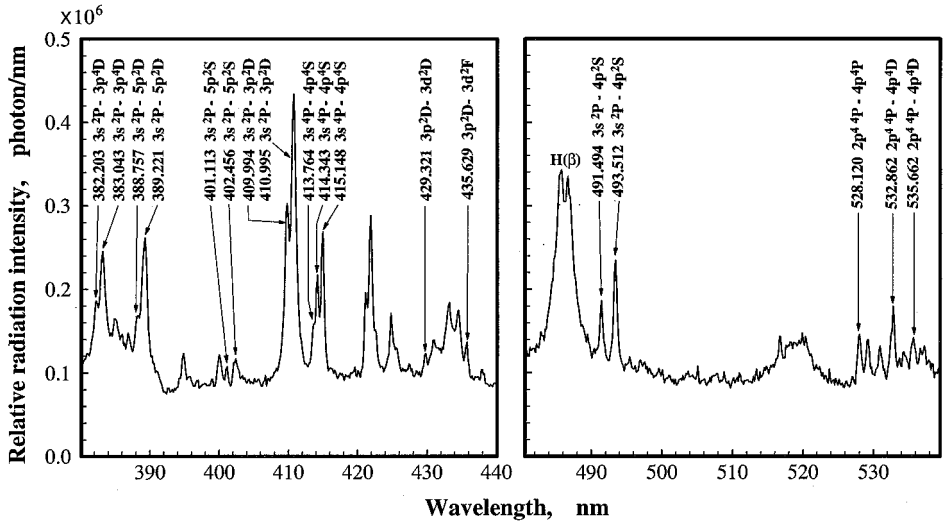

Fig. 6 Atomic lines of N at $L = 10.4 \pm 0.7$ mm (N_2 gas, $P_0 = 0.3$ torr, $V = 11.9$ km/s, and spectral resolution = 0.16 nm/pixel).

the 3-mm distance from the test plate where the boundary layer is expected to exist. In this nonuniform region the spectrum intensity was found to decrease as the distance from the test plate decreases and to increase slightly within the 1-mm distance from the test plate.

The shape of the spectrum observed in the nonuniform region was almost proportional to that obtained in the uniform region. Such trends are almost the same from the shock front to at least the middle point between the shock front and the point where the contact surface is expected to exist, although the nonuniform region extends to the 5-mm distance from the quartz plate at this middle point. Because of a small dimension of the nonuniform region compared to the uniform region and because of lower radiation intensities in the nonuniform region, the nonuniform region close to the quartz window does not have significant influences on the spectrum intensity integrated along the line of sight. Finally, the shape of the measured spectrum is expected to be the same as that of the uniform region within 10% errors.

On the other hand, the distribution of the emission spectra in the streamwise direction, which can be obtained through the repetitive measurement, is subject to the reproducibility of the shock-tube facility. The reproducibility of the shock tube is found to be excellent: the velocity deviation from the aimed value is less than 3% in general. However, because a 3% deviation of the shock velocity is found to change the radiation intensity profile along the position behind the shock wave it is possible that the thermal and chemical conditions behind the shock wave are not always the same in every measurement. Therefore, in order to obtain the temperature distribution behind the shock wave a series of spectra obtained with the measured shock velocity of $V = 11.90 \pm 0.04$ km/s are selected among a large number of experimental results.

Temperature Based on N Lines

The electronic excitation population is determined on an assumption that the radiating gas is optically thin, and the absorption process can be neglected along the line of sight. In this context the relative radiation intensity of an $i - j$ transition is proportional to the number density of the upper state i. This is the case with N lines in the wavelength ranges, 380–440 and 480–540 nm, which are selected for temperature measurement.

Figure 6 shows the observed line spectra at 10.4 ± 0.7 mm behind the shock wave ($L = 10.4 \pm 0.7$ mm). Distinguishable atomic lines of N, which are taken into consideration in determining the population, are indicated by the wavelength and the transition array. It is possible to evaluate the electronic excitation temperature by using only the lines in the 380–440-nm range (the left plot); however, those in the 480–540-nm range (the right plot) are also used to enhance the estimation accuracy. Using the transition probabilities

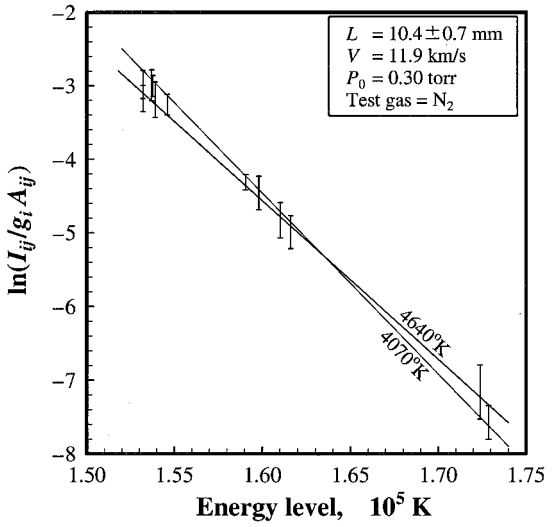

Fig. 7 Relative electronic population of N at $L = 10.4 \pm 0.7$ mm (N_2 gas, $P_0 = 0.3$ torr, and $V = 11.9$ km/s).

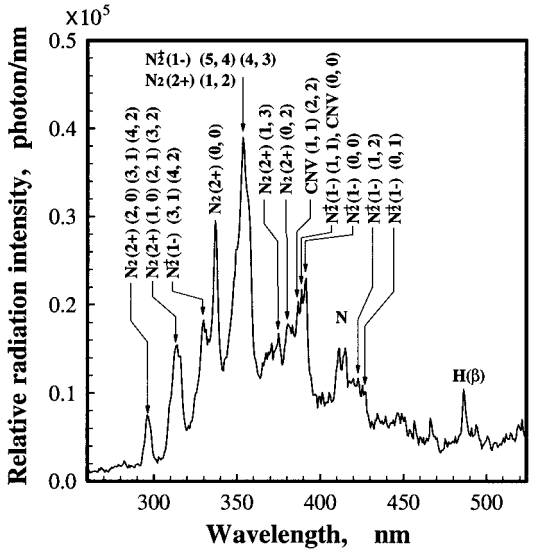

Fig. 8 Molecular spectra observed at $L = 2.6 \pm 0.7$ mm (N_2 gas, $P_0 = 0.3$ torr, $V = 11.9$ km/s, and spectral resolution = 0.69 nm/pixel).

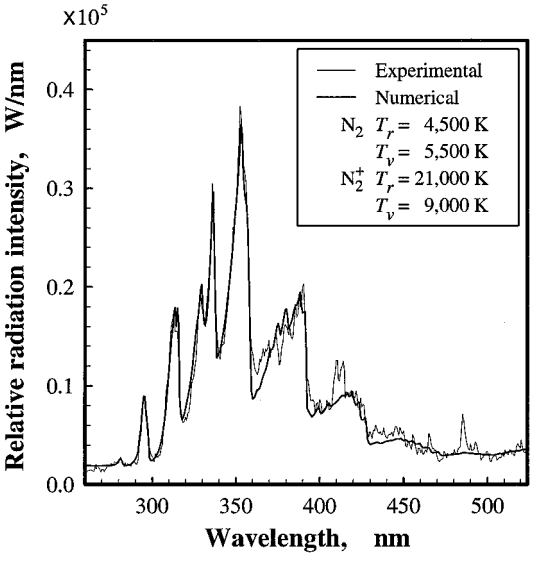

Fig. 9 Numerical fit to an observed spectrum at $L = 2.6 \pm 0.7$ mm (N_2 gas, $P_0 = 0.3$ torr, and $V = 11.9$ km/s).

taken from Ref. 11, the relative population for electronic excitation is plotted in Fig. 7 in terms of $\ln(I_{ij}/g_i A_{ij})$ against the energy level. Here, the uncertainty in the transition probability A_{ij}, which is in general less than 25% according to Ref. 11, and the errors in measuring the spectrum line intensity I_{ij} are taken into consideration for each plot. The electronic population is found to be close to the Boltzmann distribution in the range of the energy level under consideration because it is almost a linear function of the energy level. Therefore, a line fit to the plot gives the electronic excitation temperature for this distribution, which lies between 4640 and 4070°K for this case.

Temperatures Based on $N_2(2+)$ and $N_2^+(1-)$

Because of low spectral resolution in the present experiment, it is not possible to determine independently the rotational temperature from the ratio of the intensity of one rotational line to that of another. Similarly, evaluation of the vibrational temperature is not free of complications. Therefore, a trial-and-error technique based on a computer package SPRADIAN (Structured Package for Radiation Analysis[8,12]) has been developed to compute the rotational and vibrational temperatures from a composite spectrum of N_2 (2+) and N_2^+ (1−) system.

The spectral outline of molecular band spectra is dependent on the vibrational and rotational temperatures. To analyze the obtained spectra, the emission spectra of N_2 (2+) and N_2^+ (1−) system are first computed by SPRADIAN for the vibrational and rotational temperatures from 1000 to 60,000 K at every 250 K interval and then stored in an emission database. Here, the rotational–vibrational levels of each electronic state are determined by solving the vibrational Schrödinger equation, using the Rydberg–Kline–Reese potential with the molecular rotational motion incorporated.[13] An observed spectrum, which is shown in Fig. 8 for the case of $L = 2.6 \pm 0.7$ mm for example, is assumed to be a linear combination of N_2 (2+) and N_2^+ (1−) spectra, which can be reconstructed from the emission database. Thus, the most appropriate pairs of spectra, which can minimize the root-mean-square of the difference between the combined spectra and the observed one, are selected from the emission database.

A typical numerical fit to the observed spectrum of Fig. 8 is presented in Fig. 9. In this case the rotational and the vibrational temperature of N_2 are expected to be 4500 and 5500 K, respectively, whereas those of N_2^+ are 21,000 and 9000 K, respectively. The numerical spectrum is in good agreement with the measured spectrum for the range of 280–360 nm. An increased deviation found in a longer wavelength region can be accounted for by a contribution of atomic spectra originating from H and N.

Accuracy of the measured molecular temperature is estimated in the following way: when the optimum T_r and T_v are selected for the observed spectrum, the numerical spectrum is recomputed for these T_r and T_v by taking account of the uncertainty in the spectroscopic parameters. Doing so, the uncertainty of the numerical spectrum for these T_v and T_r is estimated in terms of the possible range of the rms difference between the numerical and the experimental spectrum under consideration. This range of the rms difference is then incorporated to the fitting process, and the possible range of T_r and T_v is estimated accordingly.

Spatial Distribution of Temperatures

Spatial distributions of measured temperatures are obtained as shown in Figs. 10 and 11, in which numerical predictions obtained by the two-temperature aerothermodynamic model of Park[3,4] are also shown for reference as solid curves. First of all, it can be pointed out that the measured temperatures are in significant nonequilibrium with the translational temperature, which is expected to be close to the analytical value calculated by the Park model. The electronic excitation temperature of N and the vibrational temperature of N_2 are relatively close to each other, whereas the vibrational temperature of N_2^+ is approximately two times higher. Such a higher vibrational temperature of N_2^+ is also observed by Sharma[14] at a lower shock velocity of 6.2 km/s, although the difference between the two

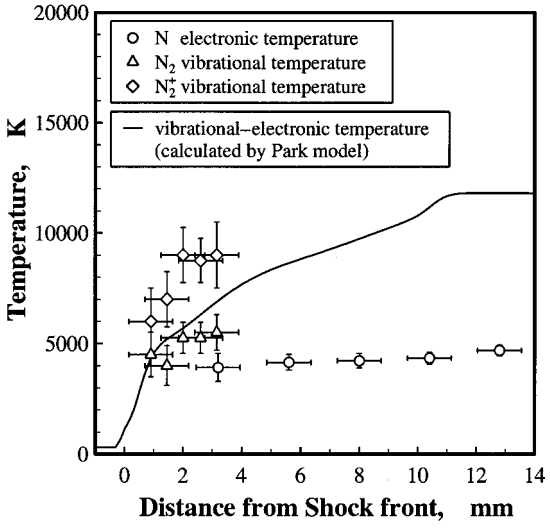

Fig. 10 Measured vibrational and electronic excitation temperatures (N_2 gas, $P_0 = 0.3$ torr, and $V = 11.9$ km/s).

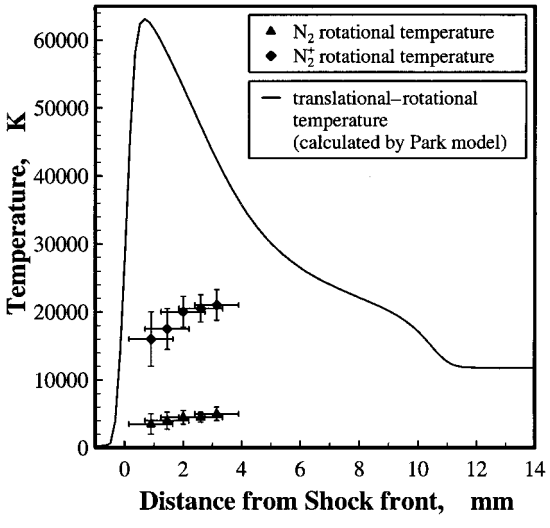

Fig. 11 Measured rotational temperatures (N_2 gas, $P_0 = 0.3$ torr, and $V = 11.9$ km/s).

vibrational temperatures is much smaller in his result than in the present measurement.

Even the rotational temperatures seem to be in significant nonequilibrium with the translational temperature, which is also the case with Sharma's results.[14] However, in the present measurement the rotational temperature of N_2 is remarkably lower than in Sharma's experiment and closer to the vibrational temperature of N_2 rather than the translational temperature. In contrast, the rotational temperature of N_2^+ is higher than that of N_2 and increases more quickly along with the distance from the shock front. The preceding results suggest a substantial departure from the two-temperature model of Park. Further investigations are necessary in the future to account for the significant temperature nonequilibrium observed immediately behind the shock front for a shock velocity as high as in the present measurement.

Conclusions

Air radiation from behind strong shock waves is observed using a free-piston double-diaphragm shock tube. A spatial variation of radiation spectra is obtained by the spatially resolved imaging spectroscopy at a shock velocity of 11.9 km/s in the ambient air at 0.3 torr. The spatial profile of the spectra is correlated with the distance from the shock front, which is detected by pressure sensors calibrated by the laser schlieren measurement. Results show that the molecular spectra of N_2 (2+) and N_2^+ (1−) system appear immediately after the shock front, whereas the atomic line spectra from N become intense shortly after it.

A series of pointwise spectroscopy is carried out in order to obtain a spatial profile of temperatures for a shock velocity of 11.9 km/s and the ambient pressure of 0.3 torr ahead of the shock wave, using pure nitrogen as the test gas. The estimated electronic excitation temperature of N is found to be approximately 4000 K at the 5-mm distance behind the shock front and to increase very gradually along with the distance from the shock front. The vibrational temperature of N_2 is close to this temperature, whereas that of N_2^+ is two times higher and quickly increases along with the distance from the shock front. The rotational temperatures of N_2 and N_2^+ are expected to be below 6500 and 23,000 K within the 3-mm distance from the shock front, respectively, which are much lower than the expected translational temperature. These results show a substantial departure from the widely used two-temperature model and imply that the region immediately after the shock front is in significant nonequilibrium, even in a viewpoint of relaxation between the translational and rotational temperatures.

Acknowledgment

The present work is partly supported by Grant-in-Aid for Encouragement of Young Scientists 09751013 at the Ministry of Education, Science, Sports and Culture, Japan.

References

[1]Gnoffo, P. A., Gupta, R. N., and Shinn, J. L., "Conservation Equations and Physical Models for Hypersonic Air Flows in Thermal and Chemical Nonequilibrium," NASA TP-2867, Feb. 1989.

[2]Gupta, R. N., Yos, J. M., Thompson, R. A., and Lee, K. P., "A Review of Reaction Rates and Thermodynamic and Transport Properties for an 11-Species Air Model for Chemical and Thermal Nonequilibrium Calculations to 30,000 K," NASA RP-1232, Aug. 1990.

[3]Park, C., *Nonequilibrium Hypersonic Aerothermodynamics,* Wiley, New York, 1990.

[4]Park, C., "Review of Chemical-Kinetic Problems of Future NASA Missions, I : Earth Entries," *Journal of Thermophysics and Heat Transfer*, Vol. 7, No. 3, 1993, pp. 385–398.

[5]Gupta, R. N., Moss, J. N., and Price, J. M., "Assessment of Thermochemical Nonequilibrium and Slip Effects for Orbital Reentry Experiment (OREX)," NASA TM-111600, July 1996.

[6]Uesugi, K., "MUSES-C Mission Plan Report," Inst. of Space and Astronautical Science, Kanagawa, Japan, March 2000.

[7]Suzuki, K., Kubota, H., Fujita, K., and Abe, T., "Chemical Nonequilibrium Ablation Analysis of MUSES-C Super-Orbital Reentry Capsule," AIAA Paper 97-2481, June 1997.

[8]Fujita, K., Abe, T., and Suzuki, K., "Air Radiation Analysis of a Superorbital Reentry Vehicle," AIAA Paper 97-2561, June 1997.

[9]Otsu, H., Suzuki, K., Fujita, K., and Abe, T., "Radiative Heating Analysis around the MUSES-C Reentry Capsule at a Superorbital Speed," AIAA Paper 98-2447, June 1998.

[10]Ogura, E., Funabiki, K., Sato, S., and Abe, T., "Free Piston Double Diaphragm Shock Tube," Inst. of Space and Astronautical Science, Rept. 96, Kanagawa, Japan, Aug. 1997.

[11]Wiese, W. L., Fuhr, J. R., and Deters, T. M., "Atomic Transition Probabilities of Carbon, Nitrogen, and Oxygen," *Journal of Physical and Chemical Reference Data,* Monograph No. 7, 1996.

[12]Fujita, K., and Takashi, A., "SPRADIAN, Structured Package for Radiation Analysis : Theory and Application," Inst. of Space and Astronautical Science, Rept. 669, Kanagawa, Japan, July 1997.

[13]Herzberg, G., *Molecular Spectra and Molecular Structure, I. Spectra of Diatomic Molecules,* reprint ed., Krieger, Malabar, FL, 1989, Chap. VII.

[14]Sharma, S. P., "Vibrational and Rotational Temperature Measurement in a Shock Tube," *Proceedings of the Eighteenth International Symposium on Shock Waves*, Vol. 1, Springer-Verlag, Berlin, 1992, pp. 683–690.